frontiers | Frontiers in Marine Science

TYPE Original Research
PUBLISHED 25 May 2023
DOI 10.3389/fmars.2023.1155979

OPEN ACCESS

EDITED BY
Shangfeng Chen,
Chinese Academy of Sciences (CAS), China

REVIEWED BY
Leticia Cotrim Da Cunha,
Rio de Janeiro State University, Brazil
Di Qi,
Jimei University, China

*CORRESPONDENCE
Xueming Zhu
zhuxueming@sml-zhuhai.cn

RECEIVED 01 February 2023
ACCEPTED 15 May 2023
PUBLISHED 25 May 2023

CITATION
Zhang M, Zhu X, Ji X, Zhang A and Zheng J (2023) Controlling factor analysis of oceanic surface pCO_2 in the South China Sea using a three-dimensional high-resolution biogeochemical model. *Front. Mar. Sci.* 10:1155979. doi: 10.3389/fmars.2023.1155979

Controlling factor analysis of oceanic surface pCO_2 in the South China Sea using a three-dimensional high-resolution biogeochemical model

Miaoyin Zhang[1,2], Xueming Zhu[3]*, Xuanliang Ji[2], Anmin Zhang[1] and Jingjing Zheng[2]

[1]School of Marine Science and Technology, Tianjin University, Tianjin, China, [2]Key Laboratory of Research on Marine Hazards Forecasting, National Marine Environmental Forecasting Center, Ministry of Natural Resources, Beijing, China, [3]Frontiers Research Center, Southern Marine Science and Engineering Guangdong Laboratory (Zhuhai), Zhuhai, China

The oceanic surface pressure of CO_2 (pCO_2) is an essential parameter for understanding the global and regional carbon cycle and the oceanic carbon uptake capacity. We constructed a three-dimensional physical-biogeochemical model with a high resolution of 1/30° for the South China Sea (SCS) to compensate for the limited temporal coverage and limited spatial resolution of the observations and numerical models. The model simulated oceanic surface pCO_2 from 1992 to 2021, and the empirical orthogonal function analysis (EOF) of the model results is conducted for a better understanding of the seasonal and interannual variations of oceanic surface pCO_2 in this region. The model results showed that the SCS serves as an atmospheric CO_2 source from March to October and a sink from November to February, with a domain-averaged climatological oceanic surface pCO_2 value that varies between 357 and 408 µatm, and the temporal variation was positively correlated with the variation of sea surface temperature (SST). The majority of the SCS showed a long-term increasing trend for oceanic surface pCO_2 with a value of (1.19±0.60) µatm/a, which is in response to the continuously rising atmospheric CO_2 concentration. The first EOF mode is positively correlated with the Niño 3 index with a correlation coefficient of 0.51 when the Niño 3 leads 5 months, and the second EOF mode is correlated with the PDO index when the PDO leads 7 months, which suggests an influence of climate variability on the carbonate system. Moreover, it was found that the long-term trend rate of oceanic surface pCO_2 was mainly controlled by total CO_2 (TCO_2) through the decomposition of influence factors, and SST variation took a dominant role in seasonal variations of pCO_2. With rapid global warming and continuous release of CO_2, the carbonate system in the SCS may change leading to calcite and aragonite saturation.

KEYWORDS

oceanic surface pCO2, sea surface temperature, total CO2, control factor, biogeochemical model

1 Introduction

Total anthropogenic CO_2 emissions have accelerated in the past few decades, and the oceanic CO_2 sink increased from 1.1 ± 0.4 GtC yr^{-1} in the 1960s to 2.8 ± 0.4 GtC yr^{-1} during the 2010s, which accounts for 23.9% and 26.4%, respectively, of the total CO_2 emissions for the same periods (Friedlingstein et al., 2022). Oceans in mid to high latitudes are a major sink zone for CO_2 due to the low temperature and high wind speed, which consequently leads to a higher gas exchange rate with a mean uptake rate of approximately 0.7 PgC yr^{-1} in the northern hemisphere. The mean uptake rate in the Northwest Pacific (NWP), for instance, is estimated to be approximately 0.5 PgC yr^{-1} and the capability of CO_2 absorption is increasing in the age of global warming (Takahashi et al., 2009; Sutton et al., 2017; Ji et al., 2022). In the absence of a clear sign of a decrease in atmospheric CO_2 concentration, the oceanic sink for CO_2 is expected to continue growing in pace with atmospheric CO_2 (McKinley et al., 2020). Oceans absorb anthropogenic CO_2 through the air-sea exchange, which shows stronger regional and seasonal variations than atmospheric CO_2 due to the direct impact of water properties (Takahashi et al., 2002; Cai et al., 2006; Chai et al., 2009). The physical and biological variables alter with the influences of solar radiation, riverine inputs, circulation pattern, wind stress, and biological production and remineralization. Essential variables such as sea surface temperature (SST), sea surface salinity (SSS), total alkalinity (TALK), total CO_2 (TCO_2), and chlorophyll concentration change and consequently affect the variability of oceanic pCO_2 (Xiu and Chai, 2014). On the seasonal time scale, oceanic surface pCO_2 is positively correlated with SST and TCO_2, whereas oceanic pCO_2 is negatively correlated with biological productivity. The climatological oceanic pCO_2 is generally high in summer and low in winter mainly due to thermodynamics, and TCO_2 contributes to the increase of oceanic surface pCO_2 in winter as a result of strong vertical transport processes that bring subsurface total inorganic carbon (TIC) to the upper layer. Upper layer TCO_2 and TALK levels are changed with biological cycles through production and remineralization, which in the end leads to variations of oceanic surface pCO_2 (Takahashi et al., 2002; Cai et al., 2004; Xiu and Chai, 2014). Moreover, on interannual and decadal scales, such long-term trend of oceanic pCO_2 varies on the basin scale and shows correlations with climate patterns (Wong et al., 2002; Dore et al., 2009; Sheu et al., 2010; Tian et al., 2019). It is challenging to determine the control factors of the oceanic surface pCO_2 due to the complex interactions among all variables.

The South China Sea (SCS) is one of the largest marginal seas in the NWP and is characterized by tropical and subtropical climates. It connects with the Pacific and the Indian Ocean through several water channels, and shares physical-biogeochemical features through upper layer exchange with the Kuroshio current and overflows at a deeper layer (Hu et al., 2000; Zhu et al., 2016). The contribution of the Kuroshio intrusion to the thermal state and ocean circulation is unneglected, which strongly affects oceanic surface pCO_2 in the northern to central SCS (Nan et al., 2015); Xu and Oey, 2015). The SCS has a complicated topography and a vast continental shelf system in the northern (Gulf of Tonkin) and southern (Gulf of Thailand and Sundan shelf) boundaries and a deep basin with a maximum depth of over 5000m (Figure 1). The SCS exhibits strong monsoon-related seasonal cycles and ENSO-related interannual patterns (Chao et al., 1996; Wong et al., 2007; He et al., 2015). Since SST makes a positive contribution to the increase of oceanic surface pCO_2, variability of the thermal state of the upper layer is crucial in understanding variations in the carbon cycle. Apart from the increased surface net heat flux, SST shows a linear warming trend since the 1990s in the SCS basin that is highly related to anomalous anticyclonic ocean circulation caused by wind stress curl (Xiao et al., 2019).

Previous studies have shown great efforts in understanding the carbon cycle by studying CO_2 flux and its control factors through observations and numerical modeling (Marinov et al., 2008; Chen et al., 2013; Laruelle et al., 2017; Tian et al., 2019; Li et al., 2020; Li et al., 2020; McKinley et al., 2020; Wang et al., 2020; Ko et al., 2021). Li et al. (2020) summarized seasonal variations of oceanic surface pCO_2 and regional features of air-sea CO_2 fluxes over the SCS based on observations from 2000 to 2018. Chai et al. (2009) used a physical-biological coupled model with a 50km resolution and concluded that SST was a dominant factor in the seasonal variation of oceanic surface pCO_2, and the influence of biological activities was also significant over the SCS. However, due to the limits of time coverage and spatial resolution of the observations and numerical models, previous studies fail to present a detailed long-term variation trend of oceanic surface pCO_2, and uncertainties remain in understanding drivers of oceanic surface pCO_2 variations on seasonal and interannual time scales over the SCS. With complex geographical and environmental conditions in the SCS, a high-resolution numerical model can help reconstruct coastal and basin-scale physical and biogeochemical status to remedy the insufficient capability for observing long-term trends of essential variables that control oceanic surface pCO_2. The

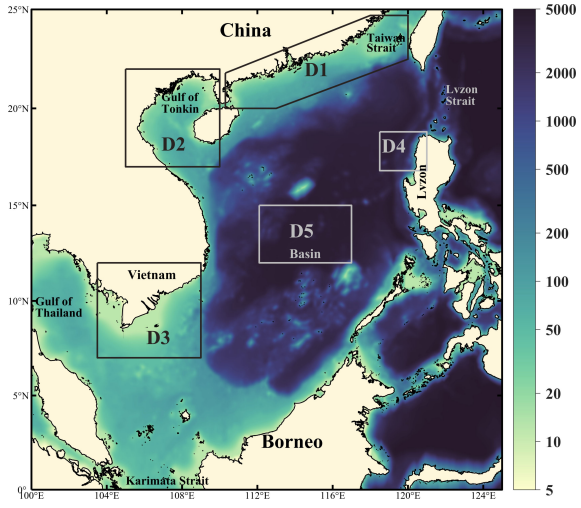

FIGURE 1
Bathymetry of the South China Sea model (unit: m). Five physical-biogeochemical domains are shown in the black/gray boxes (D1: the coast of China; D2: the Gulf of Tonkin; D3: the southern coast of Vietnam; D4: the west of Lvzon Island, and D5: the SCS basin).

physical-biological processes are complex in this region, therefore, understanding the carbon cycle in the SCS makes a positive contribution to understanding the role of marginal seas in the global carbon system and its response to climate change.

The present study is organized as follows: datasets and model settings are introduced in Section 2; the seasonal and interannual variations of oceanic surface pCO_2 are described in Section 3; the long-term trend rate of oceanic surface pCO_2 and its controlling factors are analyzed and discussed in Section 4; and conclusions are presented in section 5.

2 Data and model

2.1 Data

We introduced four sets of data in this study for model validation and long-term trend analysis of oceanic surface pCO_2. These included two sets of quality-controlled *in-situ* observation datasets to examine the capability of faithfully capturing features of oceanic surface pCO_2 variations of the model.

The monthly oceanic pCO_2 satellite dataset with a spatial resolution of 1°×1° was obtained from the Japan Meteorological Agency (JMA, datasets are accessible from their website https://www.data.jma.go.jp/gmd/kaiyou/english/co2_flux/co2_flux_data_en.html). The oceanic pCO_2 field was calculated from satellite observations of SST, SSS, and surface chlorophyll-*a* concentration (Iida et al., 2020).

Monthly *in-situ* observations of ocean surface pCO_2 were obtained from the dataset of Global Ocean Surface Carbon, which was provided by the E.U. Copernicus Marine Service Information (DOI: 10.48670/moi-00047). The data were with a resolution of 1°×1°, and the time coverage used in this study was from January 1990 to December 2021 (Chau et al., 2022).

Monthly modeled ocean surface pCO_2 came from the Global Ocean Biogeochemistry Hindcast dataset obtained from the E.U. Copernicus Marine Service Information (DOI: 10.48670/moi-00019). The datasets were based on the PISCES biogeochemical model with a resolution of 0.25°×0.25°, whose time coverage was between 1 January 1993 and 31 December 2020.

Monthly *in-situ* observations of atmospheric CO_2 concentration from Mauna Loa Observatory (MLO) (19.5°N, 155.6°W) were obtained from the Scripps Institution of Oceanography (Scripps CO_2 Program) from 1990 to 2021 (Keeling et al., 2005).

2.2 Coupled physical-biogeochemical model settings

The physical model in this study was based on the Regional Ocean Model System (ROMS) v3.7 (svn trunk revision 874 released in 2017) (Shchepetkin and McWilliams, 2005). The model configuration follows Zhu et al. (2022) in the study of the comparison and validation of ocean forecasting systems over the SCS. The model domain in this study covers 0° to 25°N and 100° to 125°E (as displayed in Figure 1) with a horizontal resolution of 1/30°, and vertical levels of 50 in σ coordinate in the upper 300m for a more sufficient resolution to resolve the thermocline well. The land-sea grid was redistributed for a better fit to the complex SCS coastline. The bathymetry was derived from the General Bathymetric Chart of the Oceans (GEBCO) global continuous terrain model for ocean and land with a 30 arcsec spatial resolution. The atmospheric forcing uses the ERA5 reanalysis dataset that has higher resolution in both spatial and temporal resolutions, and the method adopts the COARE3.0 bulk algorithm (Fairall et al., 2003) to calculate the air-sea momentum. More details about the SCS physical model configuration and simulation ability are introduced by Zhu et al. (2022).

The Carbon, Silicate, and Nitrogen Ecosystem (CoSiNE) model was used for biogeochemical stimulation in this study. Fifteen state variables were considered: four nutrients (ammonium, nitrate, silicate, and phosphate), two phytoplankton groups (picophytoplankton and diatoms), two zooplankton groups (microzooplankton and mesozooplankton), two types of chlorophyll-*a*, two types of detritus for simulating sinking and suspending, dissolved oxygen, TALK, and TCO_2. In addition, light input was considered. All the abovementioned variables used in the CoSiNE model can affect the carbonate system, which is also affected by physical processes concurrently. More detailed settings can be found in Chai et al. (2002) and Xiu and Chai (2013).

To reach a climatologically steady state of circulation model, the physical circulation model was run for a 26-year climatology state before being coupled with the biogeochemical model, and then the CoSiNE model was coupled with the physical model on the same model grid. The time step was set as 5 seconds for the external mode and 150 seconds for the internal mode.

2.3 Determining control factors of oceanic surface pCO_2

Oceanic surface pCO_2 shows a distinct positive correlation with atmospheric CO_2 concentration when the influence of anthropogenic CO_2 is taken into consideration. In addition, the variation of oceanic surface pCO_2 is also related to changes in SST, SSS, TALK, and TCO_2 according to previous studies (Takahashi et al., 2002; McKinley et al., 2006; Takahashi et al., 2009; Ji et al., 2022). To further estimate drivers of the variation rate of oceanic surface pCO_2 on the interannual time scale, we used the formula as follows to linearize the change of oceanic surface pCO_2 (Takahashi et al., 1993; McKinley et al., 2006; Xiu and Chai, 2014; Ji et al., 2022):

$$\Delta \mathrm{pCO_2} = \frac{\partial \mathrm{pCO_2}}{\partial \mathrm{SST}} \times \Delta \mathrm{SST} + \frac{\partial \mathrm{pCO_2}}{\partial \mathrm{SSS}} \times \Delta \mathrm{SSS} + \frac{\partial \mathrm{pCO_2}}{\partial \mathrm{TCO_2}} \times \Delta \mathrm{TCO_2} + \frac{\partial \mathrm{pCO_2}}{\partial \mathrm{TALK}} \times \Delta \mathrm{TALK} \quad (1)$$

To isolate variables and evaluate the influence of each control factor on the ΔpCO_2, while calculating ΔpCO_2, only the interested one control variable changes and other variables were set to their long-term mean values on the right-hand side of the above equation.

3 Results

3.1 Model validation

The SCS model was examined and validated before further analysis. Three sets of monthly oceanic pCO_2 datasets were used to compare with the SCS model result, namely, the Global Ocean Biogeochemistry Hindcast (hereinafter referred to as CMEMS_Model), the Global Ocean Surface Carbon *in-situ* observations (hereinafter referred to as CMEMS_Obs), and the satellite observations from the Japan Meteorological Agency (hereinafter referred to as JMA_Satellite). According to the time coverage of datasets, the validation period was between 1993 and 2019.

The temporal variations of monthly mean oceanic surface pCO_2 anomaly at the SEATS station (18°N, 116°E) from January 1993 to December 2019 obtained from the SCS model, CMEMS model, CMEMS observation, and JMA satellite data were compared (Figure 2). All datasets showed increasing trends of the oceanic surface pCO_2 in the SCS. The standard deviations of the increasing rates of the SCS model and CMEMS model were both low with a value of 11.60, which indicates that the SCS model can ably reconstruct and simulate the oceanic surface pCO_2 (Table 1). Validation results showed that the SCS model fits well with the temporal patterns with a generally increasing trend over time. The SCS model appeared to be greater than the observations and CMESM model, which may be related to a stronger upwelling simulation performance of the physical model.

The spatial distributions of the climatological oceanic surface pCO_2 obtained from the datasets and the SCS model all showed strong regional characteristics that the pCO_2 level is higher in the south and lower in the north, especially along the continental shelf regions (Figure 3). High pCO_2 values appear in the estuary areas (i.e., the Pearl River estuary, Red River estuary, and Mekong River estuary) due to the input of river discharge that contains a large number of nutrients and dissolved inorganic carbon (DIC) (Figures 3C, D). Due to the differences in spatial resolution of datasets, SCS model outputs showed more detailed variations in the spatial distribution of climatological oceanic surface pCO_2. Factors that influence variation and changing rate of oceanic surface pCO_2 will be discussed in the following sections. In general, the SCS model can ably reproduce variations of oceanic surface pCO_2.

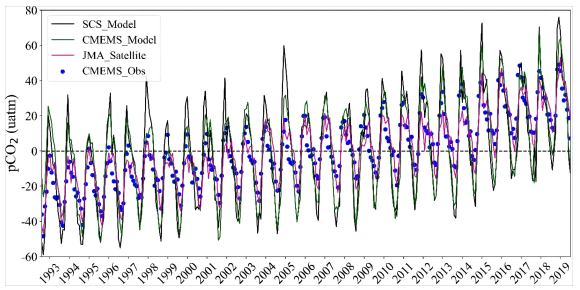

FIGURE 2
The temporal variations of the oceanic surface pCO_2 at SETAS from January 1993 to December 2019. The black line represents the SCS model output, the green line represents the CMESM model output, the blue dots represent CMESM *in-situ* observation, and the purple line represents the JMA satellite datasets, units: µatm.

3.2 Seasonal variation of oceanic surface pCO_2

The spatial distributions of oceanic surface pCO_2 and surface chlorophyll concentration, the temporal variations of atmospheric pCO_2, oceanic surface pCO_2, SST, and surface chlorophyll concentration in the SCS will be analyzed in this section, as well as the climatological seasonal variations that were obtained from the SCS modeled monthly mean values from January 1992 to December 2021. In this study, four seasons were set as follows: spring (averaged from March-April-May), summer (averaged from June-July-August), autumn (averaged from September-October-November), and winter (averaged from December-January-February).

The modeled climatological oceanic surface pCO_2 showed strong seasonal variability and regional characteristics in terms of spatial distribution (Figure 4). The regions with pCO_2 value higher than 400 µatm gradually spans from concentrating in the Karimata Strait in winter to covering the entire SCS in summer.

The oceanic surface pCO_2 decreased with the latitude from 378 µatm near the west coast of Borneo to 332 µatm on the coast of China in winter. As the annual mean atmospheric pCO_2 was 381µatm, which is derived from the MLO observations, the SCS serves as a CO_2 sink in this season. The biological productivity was more active in winter than during the other three seasons as a result of lower SST and stronger mixing process (Figures 4E–H), which consumes a massive amount of TCO_2 in water and thus intensifies the decrease of pCO_2 in the surface water (Figure 4D).

The spatial mean oceanic pCO_2 showed a slight increase to 388 µatm in spring along with the rise of seawater temperature, which suggests the SCS, in general, turns into a weak source of CO_2 in this season (Figure 4A). However, along the coast of China, the oceanic pCO_2 level was relatively low with an average value of 365 µatm in the north of 20°N, and compared to the other parts, the CO_2 fluxes were from the air to the sea in this region.

TABLE 1 The increasing rates of oceanic surface pCO_2 calculated with different datasets in the SCS from January 1993 to December 2019, units: µatm a^{-1}.

	CMEMS_Obs	CMEMS_Model	JMA_Satellite	SCS_Model
Trend rate	1.82	1.33	1.67	1.44
std	14.22	11.60	13.21	11.60

std means standard deviation.

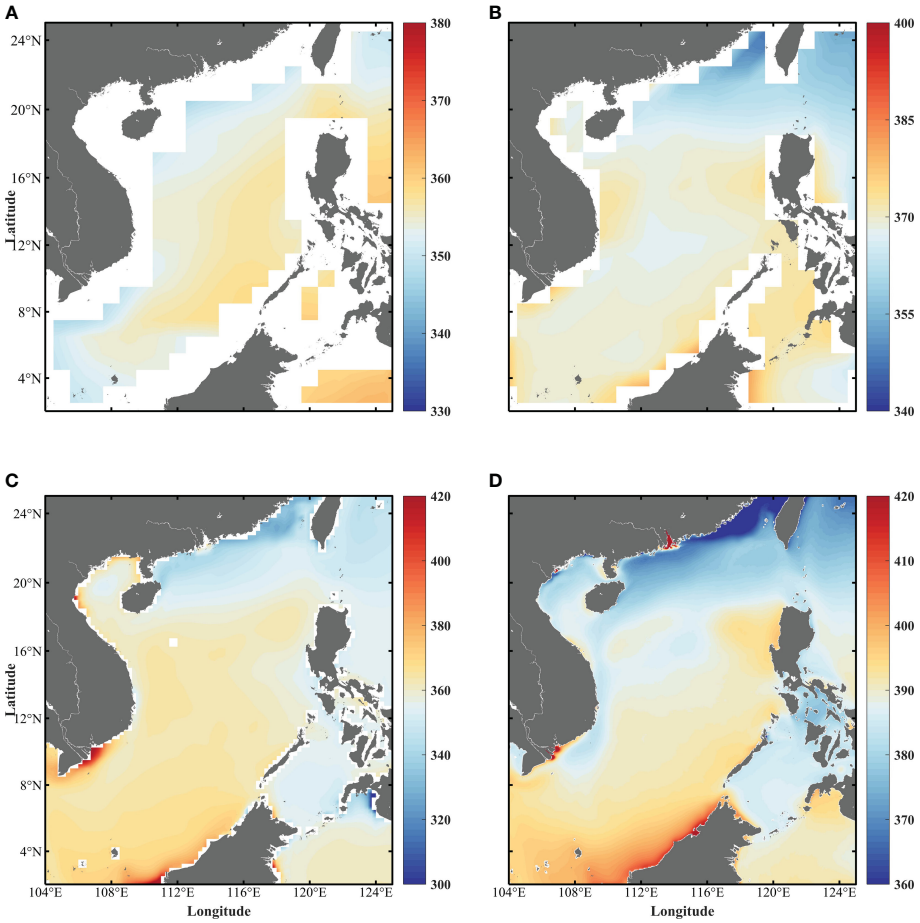

FIGURE 3
The spatial distribution of the climatological oceanic surface pCO_2 in the SCS from January 1993 to December 2019, units: µatm. **(A)** JMA satellite datasets; **(B)** CMEMS *in-situ* observation; **(C)** CMEMS model outputs; **(D)** SCS model result.

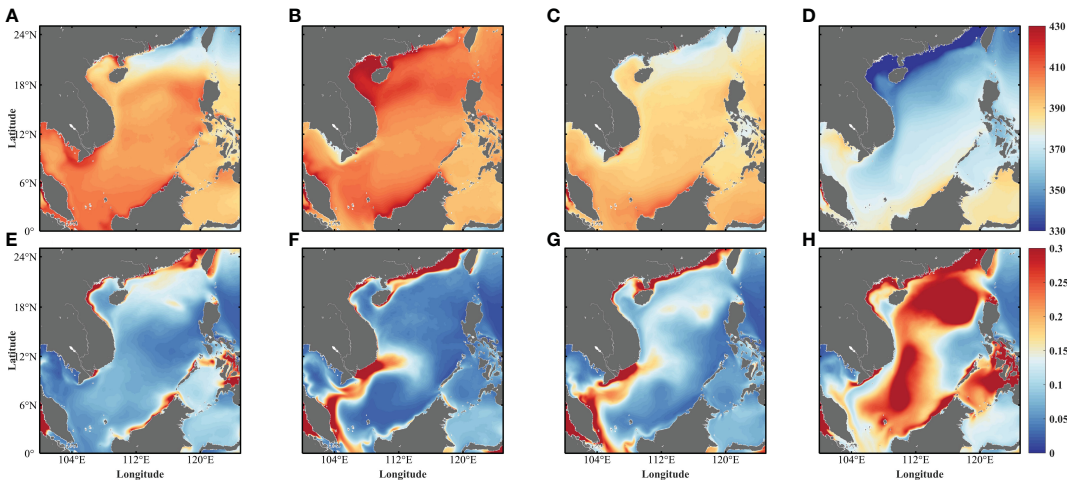

FIGURE 4
The spatial distributions of seasonal variations of the climatological oceanic surface pCO_2 (units: µatm, shown in upper panel) and chlorophyll concentration (units: mg·m^{-3}, shown in bottom panel). **(A, E)** spring, **(B, F)** summer, **(C, G)** autumn, and **(D, H)** winter.

In summer, the oceanic pCO_2 reached a domain-mean value of 400 µatm, and the maximum value of 425 µatm was spotted in the Gulf of Tonkin (Figure 4B). However, a relatively low value appeared near the southern coast of Vietnam with an oceanic pCO_2 level of 387 µatm, which was the result of the combined influence of monsoon-induced upwelling and biological productivity (Chai et al., 2009). Summer monsoon strengthens upwelling in such regions thus transporting cold water and nutrients to the surface, which enhances biological production near the coast of Vietnam; therefore, with the consumptions of TIC, the oceanic surface pCO_2 in this region appears to be lower than adjacent areas. Since the minimum value was still higher than atmospheric pCO_2, the entire SCS acts as a CO_2 source to the atmosphere in summer.

Similar to the distribution pattern in spring, the oceanic pCO_2 decreased with the increasing latitude in autumn, with an average value of 388 µatm (Figure 4C). The narrow west coast off of Borneo was with a higher value of 398 µatm; while in the northern shelf of the SCS, oceanic pCO_2 was relatively low at 377 µatm, an area that is the CO_2 sink of the SCS in autumn. Overall, the climatological oceanic surface pCO_2 spatial distribution showed strong seasonal disparity, and the regional distribution difference was in agreement with the findings by Chai et al. (2009). The mechanisms of variations of oceanic surface pCO_2 will be discussed in section 4.2.

In terms of the temporal variations of the associated oceanic surface variables, the domain-averaged climatological values of atmospheric pCO_2, oceanic pCO_2, SST, and chlorophyll-*a* concentration were compared and analyzed (Figure 5). The monthly mean oceanic pCO_2 varied between 357 and 408 µatm and peaked in June. After the peak, the decreasing rate of oceanic pCO_2 showed a slight inflection point in September (with a value of 395 µatm), with accelerated decreases afterward. The annual mean climatological atmospheric pCO_2 was around 381 µatm, indicating the SCS is a source of CO_2 into the atmosphere from March to October and a sink from November to February, which is in agreement with the findings by Wong et al. (2007). A resemblant pattern was detected in the temporal variation of SST, whose monthly mean varied between 25.6 and 29.4°C. The highest value occurred in June, followed by a slight inflection point in September (29.0°C). The seasonal cycles of SST and oceanic pCO_2 were closely linked, indicating seawater temperature positively correlates with the variation of oceanic pCO_2.

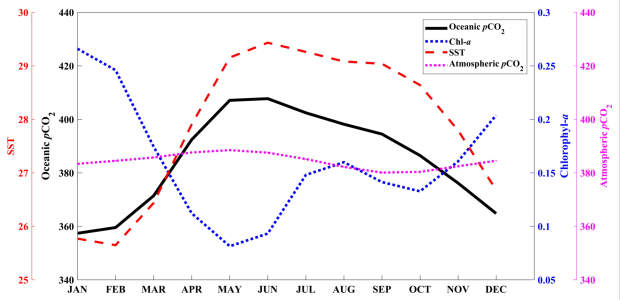

FIGURE 5
The seasonal cycles of climatological SST (units: °C, red dash line), oceanic surface pCO_2 (units: µatm, black solid line), chlorophyll-*a* concentration (units: mg·m^{-3}, blue dotted line), and atmospheric pCO_2 (units: µatm, magenta dotted line).

On the contrary, a reverse relationship between oceanic pCO_2 and chlorophyll-*a* concentration was observed. Monthly mean chlorophyll-*a* concentration varied between 0.08 and 0.27 mg m^{-3}, with a maximal value in January and a minimum value in May. The reason for the reverse patterns of chlorophyll-*a* concentration and oceanic pCO_2 is that the most active biological productivity exists in winter in the SCS, which benefits from enriched nutrients and DIC in the upper layer from the strong mixing process, therefore, more CO_2 is removed from the water by photosynthesis, thus decreasing the oceanic pCO_2; while in late spring to early summer, chlorophyll-*a* concentration drops to the bottom indicating the photosynthesis is limited by the nutrient supply. With less CO_2 being removed and higher SST, oceanic surface pCO_2 reaches the peak value in June. The modeled oceanic variable patterns were in agreement with previous studies (Liu et al., 2002; Cao et al., 2019).

The positive correlation between oceanic pCO_2 and SST and the negative correlation between oceanic pCO_2 and chlorophyll-*a* concentration suggest that the seasonal cycle of oceanic surface pCO_2 was decided by variations of SST and biological productivity in the SCS. Therefore, related variables (SST, TCO_2, TALK, and SSS) were isolated to further examine their individual effects on controlling oceanic surface pCO_2 variation, as will be discussed in section 4.

3.3 Interannual variation of oceanic surface pCO_2

Interannual and decadal variations of oceanic surface pCO_2 were examined using the Empirical Orthogonal Function (EOF) analysis. EOF analysis was first conducted on normalized oceanic surface pCO_2 without the linear trend being removed. Under such circumstances, the first EOF mode for oceanic surface pCO_2 explained 81.73% of the total variance with an increasing trend over the entire SCS (figure not shown). The correlation coefficient between the first principal component (PC1) and deseasonalized atmospheric CO_2 was 0.92, which indicates that the atmospheric CO_2 uptake significantly contributed to the increase of oceanic surface pCO_2 since the 1990s with an accelerating increase of anthropogenic CO_2 emissions. The correlation coefficients between the PC1 and normalized SST and TCO_2 were 0.69 and 0.74, respectively, which indicates tight links between oceanic pCO_2 and the abovementioned variables. The normalized oceanic surface pCO_2 and SST both showed significant increases from the year 1997 to 1998 and from 2015 to 2016, which may link with the extreme warming events in the SCS in the corresponding period (Xiao et al., 2017; Xiao et al., 2020).

As this mode explained over 80% of the total pCO_2 variance, the linear trend was removed to further examine correlations between oceanic surface pCO_2 and climatic indexes. Monthly modeled outputs from 1992 to 2021 were deseasonalized and detrended with the linear long-term trend, and the Niño 3 index and the PDO indices were introduced into the analyses to link with climate

variability for a further understanding of interannual and decadal variations of oceanic surface pCO_2.

The first EOF mode of the detrended oceanic pCO_2 appeared to be positive over the entire region, especially in the Gulf of Tonkin and the central to the southern part of the SCS, which explains 44.17% of the total variance (Figure 6A). The minimum values were distributed along the northern coast of the SCS, especially around the Pearl River plumes, which is consistent with the findings by Li et al., 2020 and Wang et al. (2020). The PC1 showed a positive response to the Niño 3 index with a correlation coefficient of 0.51 with the Niño 3 leads 5 months, which indicates an interannual modulation of oceanic surface pCO_2 by SST, and a strong influence of ENSO on the carbonate system in the SCS. The second EOF mode explained 8.16% of the total variance and exhibited a clear north-south dipole distribution (Figure 6B). The PC2 after the three-point smooth was significantly correlated with the PDO index (R=0.62) with PDO leads 7 months, which indicates there is a strong influence of the PDO on the decadal variation of the oceanic pCO_2 in the SCS. The third EOF mode explained approximately 4.48% of the total variance showing a meridional structure centered around 114°E and it could possibly relate to a mixed modulation of climate variations that need to be further investigated (Figure 6C).

4 Discussion

4.1 The trend rate of oceanic surface pCO_2

In this section, long-term trend rates of oceanic surface variables (SST, TCO_2, TALK, and SSS) were calculated and analyzed to examine their correlations with the trend rate of oceanic surface pCO_2. Due to the strong regional disparity of the abovementioned variables, the SCS was separated into five domains based on physical-biogeochemical conditions and previous studies to further explore geographical features of the various rates (Yu et al., 2019; Li et al., 2020; Wang et al., 2020). The domains were (D1) the coast of China (21.8°~24.7°E, 110.3°~120°N), (D2) the Gulf of Tonkin (17°~22°E, 105°~110°N), (D3) the southern coast of Vietnam (7°~12°E, 103.5°~109°N), (D4) the west of Lvzon Island (16.8°~18.8°E, 118.5°~121°N), and (D5) the SCS basin (12°~15°E, 112.1°~117°N). Detailed physical-biogeochemical descriptions of domains are displayed in Table 2 The water channels and confluent areas of large runoffs (here it refers to regions around the Pearl River estuary, the Red River estuary, and the Mekong River estuary) were removed from calculation to diminish the impact of runoff when examining the oceanic surface variables. The range of

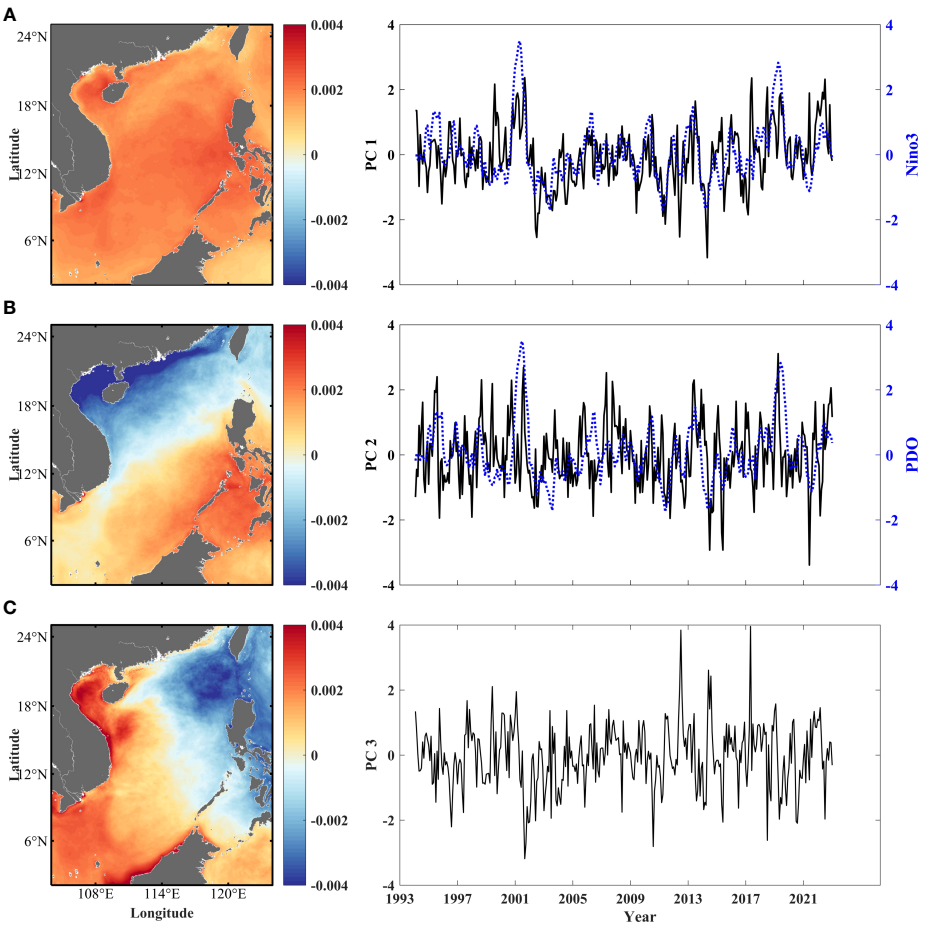

FIGURE 6
The three dominant EOF modes of the detrended oceanic surface pCO_2 (left panel) and their associated principal components (right panel). **(A)** EOF1 detrended and PC1 with the Niño3 index (5-month lag) superimposed on the PC1 mode (blue dotted line), **(B)** EOF2 detrended and PC2 with the PDO (7-month lag) superimposed on the PC2 mode (blue dotted line), **(C)** EOF3 detrended and PC3.

influence of SSS variation was limited around the estuary zone and did not show any significant regional changing trend (average value was less than 0.01 psu/a), therefore its spatial distribution is not shown in Figure 7.

Since oceanic surface pCO_2 was mainly decided by variations of SST and biological productivity, the trend rate of oceanic pCO_2 was controlled by the balance of water temperature change, upwelling and removing of TCO_2, and TALK concentration variation. Besides seasonal variations of net heat flux, carbon cycle, seawater temperature, and accompanied chlorophyll-*a* concentration variations were also associated with the coastal currents and upwelling physics in the SCS, meaning the East Asian Monsoon plays a vital role in regulating the variation of oceanic pCO_2 in this region in summer and winter (Hu et al., 2003; Xie et al., 2003; Anderson et al., 2009; Liu et al., 2010).

The modeled oceanic pCO_2, SST, and TCO_2 over the entire SCS all showed positive long-term rates of change with a domain-averaged value of 1.19 ± 0.60 μatm/a for oceanic pCO_2, 0.018 ± 0.004°C/a for SST, and 0.62 ± 0.34 mmol·m^{-3}/a for TCO_2, which were all under the influences of global warming and the increase of anthropogenic CO_2 emissions in the latest decades. A positive long-term trend rate of TALK was also observed (figure not shown); with the neglection of river discharge in this study, the TALK variation was mainly regulated by ocean currents (Yang and Byrne, 2022).

D1 and D2 are typical shelf marine systems and share common seasonal variations along the shorelines from the Taiwan Strait to the

TABLE 2 Summary of the five physical-biogeochemical domains in the SCS.

Domain	Location	Longitude (°E)	Latitude (°N)	Descriptions
D1	The coast of China	21.8~24.7	110.3~120	Region along the coast of China with water depths of less than 200 m; influenced by the Pearl River plume, coastal currents, and coastal upwelling; high chlorophyll-*a* concentration in all seasons.
D2	The Gulf of Tonkin	17~22	105~110	Shallower than 200 m; influenced by coastal currents and upwelling; high frequency of typhoon landing; higher chlorophyll-*a* level in winter.
D3	The southern coast of Vietnam	7~12	103.5~109	Influenced by the Mekong River plume and monsoon-induced eddies and upwelling.
D4	The west of Lvzon Island	16.8~18.8	118.5~121	Influenced by the winter upwelling and Kuroshio invasion; higher chlorophyll-*a* concentration in winter.
D5	The SCS basin	12~15	112.1~117	Deeper than 3000 m in general; relatively higher chlorophyll-*a* concentration in winter than in other seasons.

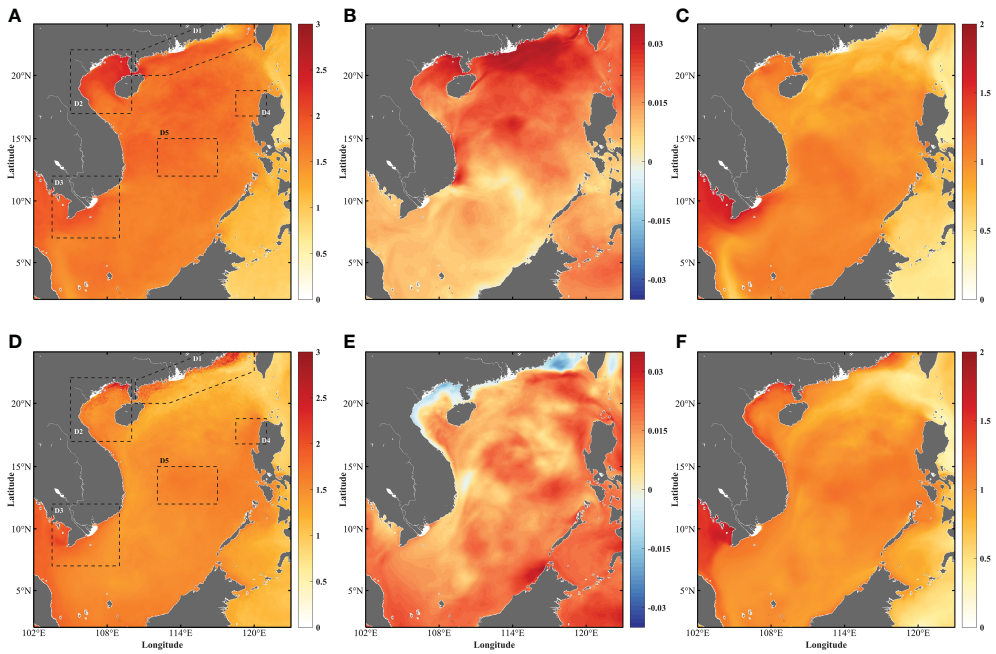

FIGURE 7
The spatial distributions of the long-term trend rates of the change of oceanic surface variables in summer (upper panel) and in winter (bottom panel). **(A, D)** oceanic surface pCO_2 change rate distribution, units: μatm·a^{-1}; **(B, E)** SST change rate distribution, units: °·a^{-1}; **(C, F)** TCO_2 change rate distribution, units: mmol·m^{-3}·a^{-1}. The five physical-biogeochemical domains are shown in black dotted boxes in **(A)**.

Gulf of Tonkin. The modeled SST trend rate was high in summer and low in winter in both regions (Figures 7B, E; Table 3) with a peak value among all five regions of 0.029 ± 0.005°C/a in summer in D1, and a runner-up value of 0.021 ± 0.006°C/a appearing in D2, which is in agreement with the findings by Yu et al. (2019). The warming trend leads to an intensification of stratification of the water column, therefore inhibiting the increase of TCO_2 in return, so the trend rate of TCO_2 was lower in summer than in winter in both regions (Figures 7C, F; Table 3). Under the combined influences of a strong warming trend of SST and a weak increasing trend of TCO_2, the oceanic surface pCO_2 trend rates were much higher in summer than in winter in both regions, the differences between the two seasons were 0.35 µatm/a and 0.43 µatm/a, respectively (Figures 7A, D; Table 3). Therefore, in the shelf system, SST makes a greater contribution to the increase of oceanic surface pCO_2 in summer, and TCO_2 accounts for a positive trend in both seasons.

In D3, owing to the prevailing monsoon system over the SCS, oceanic variables showed pronounced seasonality. In summer, the southwesterly monsoon strengthened the upwelling near the shoreline, and the increasing trend of TCO_2 and TALK were both observed in summer in this region (Table 3), which is under the influence of monsoon-induced upwelling that brings cold water, TCO_2, and nutrients in the subsurface layer up to the upper layer (Xie et al., 2003; Jing et al., 2016). Whereas, the modeled SST exhibited a "cold gyre" showing a slightly decreasing trend (Figure 7B), which may be related to the Vietnam cold eddies induced by monsoon and land topography (Yuan et al., 2005; Hu et al., 2011; Valsala and Murtugudde, 2015). In winter, with the prevailing wind turning northeasterly, upwelling along the Vietnam coast was weakened, which brought a relatively warmer trend of SST in the extended area (Table 3). With the inhibiting effect of high SST and consumption from biological production and remineralization, TCO_2 and TALK as a result showed weak increasing rates (Figure 4H; Table 3). The oceanic pCO_2 maintained a high increasing trend rate in the summer and low in the winter, which suggests it is dominated by the variation of TCO_2 (this will be further illustrated in section 4.2).

The northeasterly monsoon wind promoted upwelling effects in D4 and D5 in winter; nutrients and TCO_2 were transported to the upper layer, which contributed to the increase in the trend rate of TCO_2 (Chen et al., 2022). In addition, the intrusion of the Kuroshio current in the SCS peaks from the fall to January, which contributes to a higher increasing rate of SST from Lvzon Strait to the west of the SCS in winter (Xue et al., 2004; Nan et al., 2015). However, the trend rate of TCO_2 around the west off Lvzon Island (D4) was lower in winter even with the positive influence of monsoon-induced upwelling (Table 3), and the reason is that the biological productivity is significant (the average value of chlorophyll-*a* concentration is over 0.3 mg/m^3), and it balances out the positive effect of upwelling, resulting in a weakened TCO_2 increase in winter; while the promoting effect of monsoon-induced upwelling gradually recedes in summer, which benefits the increasing trend of TCO_2 due to the weakened biological productivity in D4. The long-term trend rates of oceanic variables were relatively stable in D5 as an abysmal region (Table 3).

Overall, among the five typical regions, the trend rate of oceanic surface pCO_2 was mainly controlled by the balance between SST variations, and input and removal of TCO_2. Therefore, control factors for long-term oceanic surface pCO_2 trend rate will be discussed through influence factor decomposition in the next section by focusing on the effects of SST and TCO_2 from region to region.

4.2 Drivers for long-term oceanic surface pCO_2 trends in different regions

Control factors including SST, TCO_2, TALK, and SSS were examined to determine the critical factor influencing the long-term trend rate of oceanic surface pCO_2 following Equation (1). The contributions from each variable were analyzed, and negative values of pCO_2-TALK and pCO_2-SSS were detected in most of the regions (Table 4). The effects of pCO_2-TALK and pCO_2-SSS were mainly the reflections of precipitation, evaporation, riverine inputs, and

TABLE 3 Long-term trend rates of oceanic surface pCO_2, SST, TCO_2, and TALK in summer and winter in the five physical-biogeochemical domains.

Region	Season	pCO_2 (µatm·a^{-1})	SST (°C·a^{-1})	TCO_2 (mmol·m^{-3}·a^{-1})	TALK (mmol·m^{-3}·a^{-1})	SSS (mmol·m^{-3}·a^{-1})
D1_Coast	summer	1.700 ± 0.301	0.029 ± 0.005	0.736 ± 0.123	0.144 ± 0.114	-0.003 ± 0.007
	winter	1.343 ± 0.366	0.006 ± 0.011	0.837 ± 0.224	0.156 ± 0.061	-0.004 ± 0.003
D2_Tonkin	summer	2.001 ± 0.236	0.021 ± 0.006	1.018 ± 0.084	0.244 ± 0.088	-0.006 ± 0.005
	winter	1.568 ± 0.218	0.005 ± 0.01	1.120 ± 0.149	0.321 ± 0.086	-0.004 ± 0.003
D3_Vietnam	summer	1.658 ± 0.117	0.011 ± 0.004	1.089 ± 0.142	0.351 ± 0.105	-0.004 ± 0.003
	winter	1.475 ± 0.106	0.013 ± 0.004	0.983 ± 0.065	0.28 ± 0.032	-0.005 ± 0.002
D4_Lvzon	summer	1.632 ± 0.051	0.016 ± 0.002	0.986 ± 0.032	0.296 ± 0.021	-0.005 ± 0.001
	winter	1.565 ± 0.091	0.020 ± 0.004	0.98 ± 0.079	0.298 ± 0.031	-0.005 ± 0.002
D5_Basin	summer	1.721 ± 0.062	0.016 ± 0.004	1.032 ± 0.063	0.302 ± 0.025	-0.003 ± 0.002
	winter	1.582 ± 0.039	0.016 ± 0.004	1.085 ± 0.04	0.350 ± 0.021	-0.006 ± 0.001

the ± values are the standard deviations of the region mean.

biological removal (Huang et al., 2015; Huang et al., 2021). By comparing to influences of pCO_2-SST and pCO_2-TCO_2, their contributions to the change rate of oceanic pCO_2 were insignificant (Xiu and Chai, 2014; Sutton et al., 2017), therefore only drivers of pCO_2-SST and pCO_2-TCO_2 in summer and winter are shown in Figure 8.

δpCO_2 showed an increasing trend in the SCS with a domain-average value of 0.54 μatm/a in summer and 0.45 μatm/a in winter. The δpCO_2 had a higher increasing rate in the north to the central SCS in summer; while in winter, the high trend value was mainly distributed in the shallow waters along the shorelines of China (Figures 8A, D). All five domains showed higher values of δpCO_2 in summer than in winter, which corresponded to the long-term trend rate of pCO_2. The trend of δpCO_2 in the Gulf of Tonkin achieved the maximum value within the five domains with values of 0.735 ± 0.191 μatm/a in summer and 0.636 ± 0.159 μatm/a in winter, which indicates that the ocean releases more CO_2 to the air in this region.

The contribution of SST to the trend rate of oceanic pCO_2 was consistent with the trend rate of SST in most regions, whose influence on the trend rate of oceanic pCO_2 was 33.85% in summer and 34.86% in winter. The positive trend rate of pCO_2-SST covered most of the regions in both seasons (Figures 8B, E), and negative trend rates were seen in the Taiwan Strait and around the west of Lvzon Island in winter, which indicates a decreasing trend of oceanic pCO_2 due to the reduction of SST trend rates (Figures 7E, 8E). The contribution of TCO_2 dominated the SCS in both seasons, whose influence on the trend rate of oceanic pCO_2 was 83.67% in summer and 87.93% in winter, indicating that TCO_2 is the major driver for the long-term trend of oceanic surface pCO_2 (Figures 8C, F).

In D1, the correlation coefficient between the trend rate of oceanic pCO_2 and the trend rate of pCO_2-SST was 0.23 in summer and 0.20 in winter, while the correlation coefficient between the trend rate of pCO_2 and the trend rate of pCO_2-TCO_2 was 0.46 in summer (accounting for 65.98% of oceanic pCO_2) and 0.86 in winter (accounting for 74.85% of oceanic pCO_2). Hence, the trend rate of pCO_2-TCO_2 was more decisive than the trend rate of pCO_2-SST in the shelf marine system, where the trend rate of oceanic pCO_2 was mainly influenced by coastal currents and coastal upwelling effects.

The domain D2 was with the largest trend rate value of oceanic pCO_2 in the five domains with a value of 0.735 ± 0.191 μatm/a, and the trend rate of pCO_2-TCO_2 accounted for 0.689 ± 0.151 μatm/a, suggesting its predominant function. On the other hand, the influence of SST was low in summer, which only accounted for 29.39% of the trend rate of oceanic pCO_2 (Table 4). The possible mechanisms are not certain yet, one possible cause may link with a high frequency of typhoon landing in this region in summer, with strong wind stress, heavy rainfall, intensified mixing effects, and accelerated air-sea exchange (Potter et al., 2017; Ko et al., 2021), hence resulting in a low contribution of pCO_2-SST and a high contribution of pCO_2-TCO_2. Further analysis and investigation are required on this subject in the future.

In D3, the seasonal variations of the trend rate of pCO_2-SST and pCO_2-TCO_2 were dominated by the East Asian Monsoon and had similar seasonal patterns as the variations of the trend rates of SST and TCO_2. The pCO_2-TCO_2 accounted for 94.55% of the trend rate of oceanic pCO_2 in summer and 89.17% in winter, indicating the predominance of TCO_2 in controlling the long-term trend rate of pCO_2 (Table 4).

The influence of TCO_2 in D4 and D5 was significant in winter, pCO_2-TCO_2 accounted for 101.97% in D4 and 105.68% in D5, as a result of the strong positive impact of monsoon-induced upwelling on TCO_2 (Table 4). Gyre structures distributed in the west of Lvzon Island were spotted (Figures 8E, F), which indicates abnormal values appeared for the trend rate of pCO_2-SST and pCO_2-TCO_2 in winter. This may correspond to mesoscale eddies or anomalous wind stress curl over the region (Guo et al., 2015; Xiao et al., 2019), and it is worth further analyzing the relationships between oceanic surface pCO_2 and mesoscale structures in future research work.

TABLE 4 Long-term trend rates of pCO_2 under influences of SST, TCO_2, TALK, and SSS in summer and winter in the five physical-biogeochemical domains.

Region	Season	δpCO_2	pCO_2-SST	pCO_2-TCO_2	pCO_2-TALK	pCO_2-SSS
		($\mu atm \cdot a^{-1}$)	($\mu atm \cdot a^{-1}$)	($\mu atm \cdot a^{-1}$)	($\mu atm \cdot a^{-1}$)	($\mu atm \cdot a^{-1}$)
D1_Coast	summer	0.582 ± 0.246	0.244 ± 0.061	0.384 ± 0.393	0.135 ± 1.005	-0.181 ± 0.393
	winter	0.497 ± 0.195	0.199 ± 0.147	0.372 ± 0.301	—	—
D2_Tonkin	summer	0.735 ± 0.191	0.216 ± 0.074	0.689 ± 0.151	-0.077 ± 0.087	-0.094 ± 0.112
	winter	0.636 ± 0.159	0.266 ± 0.075	0.51 ± 0.152	-0.074 ± 0.103	-0.066 ± 0.115
D3_Vietnam	summer	0.569 ± 0.073	0.178 ± 0.039	0.538 ± 0.121	-0.130 ± 0.100	—
	winter	0.471 ± 0.432	0.184 ± 0.041	0.420 ± 0.078	-0.097 ± 0.295	—
D4_Lvzon	summer	0.701 ± 0.061	0.312 ± 0.043	0.480 ± 0.038	-0.093 ± 0.017	—
	winter	0.508 ± 0.062	0.158 ± 0.031	0.518 ± 0.060	-0.142 ± 0.018	—
D5_Basin	summer	0.667 ± 0.021	0.230 ± 0.030	0.600 ± 0.0450	-0.121 ± 0.019	—
	winter	0.511 ± 0.030	0.158 ± 0.033	0.540 ± 0.034	-0.158 ± 0.013	—

the ± values are the standard deviations of the region mean. — indicates no visible trend, whose criteria value is 0.05.

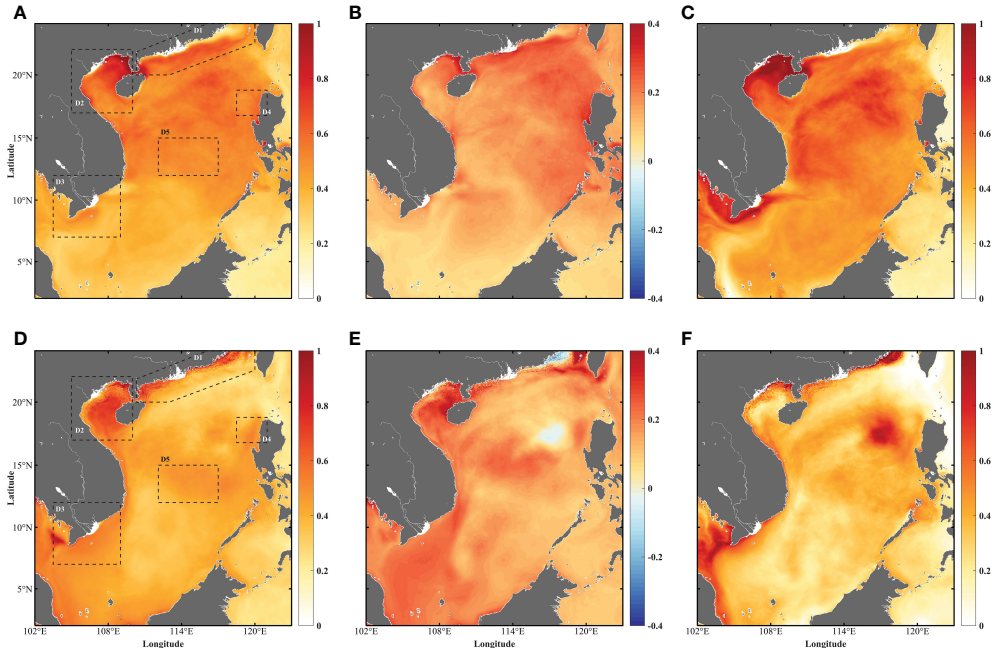

FIGURE 8
The spatial distributions of the long-term trend rates of change of pCO_2 in summer (upper panel) and in winter (lower panel), units: μatm·a^{-1}. **(A, D)** pCO_2; **(B, E)** pCO_2-SST; **(C, F)** pCO_2-TCO_2. The five physical-biogeochemical domains are shown in black dotted boxes.

5 Conclusion

This study simulates oceanic surface pCO_2 in the SCS based on a three-dimensional physical-biogeochemical model for a better understanding of the seasonal and interannual variations of oceanic surface pCO_2, and drivers that regulate the variations in this region. Based on the results from the SCS model between 1992 and 2021, a stable increasing trend of oceanic surface pCO_2 was detected over the entire SCS, and the trend was tightly linked with global warming and the increase of atmospheric CO_2 emissions. The temporal variation of climatological oceanic surface pCO_2 varied between 357 and 408 μatm, and results showed that the SCS serves as a source of CO_2 from March to October, and a sink of CO_2 during the rest of the year. The oceanic surface pCO_2 showed a positive correlation with SST and TCO_2 and a negative correlation with chlorophyll-*a* concentration. On the interannual time scale, the Niño 3 index and the PDO index correlated with the first and second principal components of the detrended oceanic pCO_2, which indicates the influences of ENSO and other climate variations on the oceanic pCO_2 variation.

The trend rate of oceanic surface pCO_2 was mainly affected by SST variations and input and removal of TCO_2. In the shelf system (D1 and D2), the variation of oceanic pCO_2 was more strongly correlated with SST (especially in the summer) as a result of a stronger warming trend of SST and a weaker increasing trend of TCO_2 in summer, and TCO_2 was positively correlated with oceanic pCO_2 variation in both summer and winter. In areas dominated by the East Asian monsoon (D3, D4, and D5), the monsoon-induced upwelling promoted the increase of TCO_2 in the surface water, and the change of the trend rate of oceanic pCO_2 was mainly controlled by the input and removal of TCO_2.

The positive trend rate of δpCO_2 was detected in the whole region with a higher value in summer and a lower value in winter. It was found that TCO_2 and SST both contribute positively to the increase of the trend rate of δpCO_2, while TALK and SSS show negative contributions in most domains through the influence factor decomposition. The influence of TCO_2 on δpCO_2 was significantly greater than that of SST in all domains, which indicates that TCO_2 is the major driver for the variation of the long-term trend rate of oceanic surface pCO_2.

The seasonal and interannual variations of oceanic surface pCO_2 and drivers that regulate the variations were analyzed. The analyses showed that the oceanic pCO_2 is mainly controlled by TCO_2 on the seasonal scale and responds to ENSO and other climate variability on the interannual scale. Furthermore, the atmospheric CO_2 uptake makes a significant contribution to the increase of oceanic pCO_2 on decadal timescales, therefore understanding the carbon cycle in the SCS helps to better explain the role of marginal seas in the global carbon system in the age of climate change. With more uncertainties that climate change brings, the carbonate system in the SCS may continue to change, and it is worthy of further investigation and research.

Data availability statement

The raw data supporting the conclusions of this article will be made available by the authors, without undue reservation.

Author contributions

MZ analyzed the data and wrote the original draft. XZ performed the physical model and free-run simulations. XJ designed the study and helped with reading over and polishing the paper. AZ and JZ contributed to the manuscript. All authors approved the submitted version.

Funding

The research was supported by the project of Southern MarineScience and Engineering Guangdong Laboratory (Zhuhai) (nos.SML2020SP008), the National Key R&D Program of China (2022YFC3105102), and the National Natural Science Foundationof China (nos. 42176029).

Acknowledgments

This work has benefited from open access to numerous datasets provided by the E.U. Copernicus Marine Service Information, including monthly global ocean surface carbon observations (Available at: https://data.marine.copernicus.eu/product/GLOBAL_MULTIYEAR_BGC_001_029/description) and model outputs of global Biogeochemistry hindcast (Available at: https://data.marine.copernicus.eu/product/GLOBAL_MULTIYEAR_BGC_001_029/description). The monthly oceanic pCO_2 grided satellite observation was obtained from the Japan Meteorological Agency (JMA Ocean CO_2 Map) and is available at: https://www.data.jma.go.jp/gmd/kaiyou/english/co2_flux/co2_flux_data_en.html. The monthly atmospheric CO_2 concentration *in-situ* observation was obtained from the Scripps Institution of Oceanography (Scripps CO_2 Program) and is available at: https://scrippsco2.ucsd.edu/data/atmospheric_co2/mlo.html.

Conflict of interest

The authors declare that the research was conducted in the absence of any commercial or financial relationships that could be construed as a potential conflict of interest.

Publisher's note

References

Anderson, R. F., Ali, S., Bradtmiller, L. I., Nielsen, S. H. H., Fleisher, M. Q., Anderson, B. E., et al. (2009). Wind-Driven Upwelling in the Southern Ocean and the Deglacial Rise in Atmospheric CO2. *Science* (*New York, N.Y.*) 323, 1443–1448. doi: 10.1126/science.1167441

Cai, W.-J., Dai, M., and Wang, Y. (2006). Air-sea exchange of carbon dioxide in ocean margins: a province-based synthesis. *Geophys. Res. Lett.* 33. doi: 10.1029/2006GL026219

Cai, W.-J., Dai, M., Wang, Y., Zhai, W., Huang, T., Chen, S., et al. (2004). The biogeochemistry of inorganic carbon and nutrients in the pearl river estuary and the adjacent northern south China Sea. *Continental Shelf Res.* 24, 1301–1319. doi: 10.1016/j.csr.2004.04.005

Cao, Z., Yang, W., Zhao, Y., Guo, X., Yin, Z., Chuanjun, D., et al. (2019). Diagnosis of CO2 dynamics and fluxes in global coastal oceans. *Natl. Sci. Rev.* 7, 786–797. doi: 10.1093/nsr/nwz105

Chai, F., Dugdale, R., Peng, T. H., Wilkerson, F., and Barber, R. (2002). One-dimensional ecosystem model of the equatorial pacific upwelling system. part I: model development and silicon and nitrogen cycle. *Deep Sea Res. Part II: Top. Stud. Oceanog.* 49, 2713–2745. doi: 10.1016/S0967-0645(02)00055-3

Chai, F., Liu, G., Xue, H., Shi, L., Chao, Y., Tseng, C.-M., et al. (2009). Seasonal and interannual variability of carbon cycle in south China Sea: a three-dimensional physical-biogeochemical modeling study. *J. Oceanog.* 65, 703–720. doi: 10.1007/s10872-009-0061-5

Chao, S.-Y., Shaw, P.-T., and Wu, S. Y. (1996). Deep water ventilation in the south China Sea. *Deep Sea Res. Part I: OceanograpH. Res. Pap.* 43, 445–466. doi: 10.1016/0967-0637(96)00025-8

Chau, T. T. T., Gehlen, M., and Chevallier, F. (2022). A seamless ensemble-based reconstruction of surface ocean pCO2 and air–sea CO2 fluxes over the global coastal and open oceans. *Biogeosciences* 19, 1087–1109. doi: 10.5194/bg-19-1087-2022

Chen, C. T. A., Huang, T. H., Chen, Y. C., Bai, Y., He, X., and Kang, Y. (2013). Air–sea exchanges of CO2 in the world's coastal seas. *Biogeosciences* 10, 6509–6544.10.5194/bg-10-6509-2013. doi: 10.5194/bg-10-6509-2013

Chen, M., Zhao, X., Li, D.-W., and Dong, L. (2022). Mesoscale Eddy Effects on Nitrogen Cycles in the Northern South China Sea Since the Last Glacial. *Front. Earth Sci.* doi: 10.10.3389/feart.2022.886200

Dore, J. E., Lukas, R., Sadler, D. W., Church, M. J., and Karl, D. M. (2009). Physical and biogeochemical modulation of ocean acidification in the central north pacific. *Proc. Natl. Acad. Sci. USA* 106, 12235–12240. doi: 10.1073/pnas.0906044106

Fairall, C. W., Bradley, E. F., Hare, J. E., Grachev, A. A., and Edson, J. B. (2003). Bulk parameterization of air–Sea fluxes: updates and verification for the COARE algorithm. *J. J. Climate* 16, 571–591. doi: 10.1175/1520-0442(2003)016<0571:Bpoasf>2.0.Co;2

Friedlingstein, P., Jones, M. W., O'Sullivan, M., Andrew, R. M., Bakker, D. C. E., Hauck, J., et al. (2022). Global carbon budget 2021. *Earth Syst. Sci. Data* 14, 1917–2005. doi: 10.5194/essd-14-1917-2022

GEBCO *GEBCO_2014 grid [data set]*. Available at: https://www.gebco.net/data_and_products/historical_data_sets/#gebco_2014 (Accessed 12 December 2022).

Guo, M., Chai, F., Xiu, P., Li, S., and Rao, S. (2015). Impacts of mesoscale eddies in the south China Sea on biogeochemical cycles. *Ocean Dynam.* 65, 1335–1352. doi: 10.1007/s10236-015-0867-1

He, Y., Cai, S., Wang, D., and He, J. (2015). A model study of Luzon cold eddies in the northern south China Sea. *Deep Sea Res. Part I: OceanograpH. Res. Pap.* 97, 107–123. doi: 10.1016/j.dsr.2014.12.007

Hu, J., Gan, J., Sun, Z., Zhu, J., and Dai, M. (2011). Observed three-dimensional structure of a cold eddy in the southwestern south China Sea. *J. Geophys. Res.* 116. doi: 10.1029/2010jc006810

Hu, J., Kawamura, H., Hong, H., and Qi, Y. (2000). A review on the currents in the south China Sea: seasonal circulation, south China Sea warm current and kuroshio intrusion. *J. Oceanog.* 56, 607–624. doi: 10.1023/A:1011117531252

Hu, J. Y., Kawamura, H., and Tang, D. L. (2003). Tidal front around the hainan island, northwest of the south China Sea. *J. Geophys. Res. Oceans* 108, 3342. doi: 10.1029/2003jc001883

Huang, W.-J., Cai, W.-J., and Hu, X. (2021). Seasonal mixing and biological controls of the carbonate system in a river-dominated continental shelf subject to eutrophication and hypoxia in the northern gulf of Mexico. *Front. Mar. Sci.* 8. doi: 10.3389/fmars.2021.621243

Huang, W. J., Cai, W. J., Wang, Y., Lohrenz, S. E., and Murrell, M. C. (2015). The carbon dioxide system on the Mississippi river-dominated continental shelf in the northern gulf of Mexico: 1. distribution and air-sea CO(2) flux. *J. Geophys Res. Ocean.* 120, 1429–1445. doi: 10.1002/2014JC010498

Iida, Y., Takatani, Y., Kojima, A., and Ishii, M. (2021). Global trends of ocean CO2 sink and ocean acidification: an observation-based reconstruction of surface ocean inorganic carbon variables. *J. Oceanog.* 77, 323–358. doi: 10.1007/s10872-020-00571-5

Ji, X., Chai, F., Xiu, P., and Liu, G. (2022). Long-term trend of oceanic surface carbon in the Northwest pacific from 1958 to 2017. *Acta Oceanol. Sin.* 41, 90–98. doi: 10.1007/s13131-021-1953-5

Jing, Z., Qi, Y., Fox-Kemper, B., Du, Y., and Lian, S. (2016). Seasonal thermal fronts on the northern south China Sea shelf: satellite measurements and three repeated field surveys. *J. Geophys. Res.: Ocean.* 121, 1914–1930. doi: 10.1002/2015JC011222

Keeling, C. D., Piper, S. C., Bacastow, R. B., Wahlen, M., Whorf, T. P., Heimann, M., et al. (2005). "Atmospheric CO2 and 13CO2 exchange with the terrestrial biosphere and oceans from 1978 to 2000: observations and carbon cycle implications," in *A history of atmospheric CO2 and its effects on plants, animals, and ecosystems*. Eds. I. T. Baldwin, M. M. Caldwell, G. Heldmaier, R. B. Jackson, O. L. Lange, H. A. Mooney, et al (New York, NY: Springer New York).

Ko, Y. H., Park, G.-H., Kim, D., and Kim, T.-W. (2021). Variations in seawater pCO2 associated with vertical mixing during tropical cyclone season in the northwestern subtropical pacific ocean. *Front. Mar. Sci.* 8. doi: 10.3389/fmars.2021.679314

Laruelle, G. G., Landschützer, P., Gruber, N., Tison, J.-L., Delille, B., and Regnier, P. (2017). Global high-resolution monthly pCO2 climatology for the coastal ocean derived from neural network interpolation. *Biogeosciences* 14, 4545–4561.10.5194/bg-14-4545-2017. doi: 10.5194/bg-14-4545-2017

Li, Q., Guo, X., Zhai, W., Xu, Y., and Dai, M. (2020). Partial pressure of CO2 and air-sea CO2 fluxes in the south China Sea: synthesis of an 18-year dataset. *Prog. Oceanog.* 182, 102272. doi: 10.1016/j.pocean.2020.102272

Liu, K. K., Chao, S. Y., Shaw, P. T., Gong, G. C., Chen, C. C., and Tang, T. Y. (2002). Monsoon-forced chlorophyll distribution and primary production in the south China Sea: observations and a numerical study. *Deep Sea Res. Part I: OceanograpH. Res. Pap.* 49, 1387–1412. doi: 10.1016/S0967-0637(02)00035-3

Liu, S. M., Guo, X., Chen, Q., Zhang, J., Bi, Y. F., Luo, X., et al. (2010). Nutrient dynamics in the winter thermohaline frontal zone of the northern shelf region of the south China Sea. *J. Geophys. Res.* 115, C11020. doi: 10.1029/2009jc005951

Marinov, I., Gnanadesikan, A., Sarmiento, J. L., Toggweiler, J. R., Follows, M., and Mignone, B. K. (2008). Impact of oceanic circulation on biological carbon storage in the ocean and atmosphericpCO2. *Global Biogeochem. Cycles* 22, n/a–n/a. doi: 10.1029/2007gb002958

McKinley, G., Fay, A., Eddebbar, Y., Gloege, L., and Lovenduski, N. (2020). External forcing explains recent decadal variability of the ocean carbon sink. *AGU Adv.* 1, e2019AV000149. doi: 10.1029/2019AV000149

McKinley, G. A., Takahashi, T., Buitenhuis, E., Chai, F., Christian, J. R., Doney, S. C., et al. (2006). North pacific carbon cycle response to climate variability on seasonal to decadal timescales. *J. Geophys. Res.* 111, C07S06. doi: 10.1029/2005jc003173

Nan, F., Xue, H., and Yu, F. (2015). Kuroshio intrusion into the south China Sea: a review. *Prog. Oceanog.* 137, 314–333. doi: 10.1016/j.pocean.2014.05.012

Potter, H., Drennan, W. M., and Graber, H. C. (2017). Upper ocean cooling and air-sea fluxes under typhoons: a case study. *J. Geophys. Res. Oceans* 122, 7237–7252. doi: 10.1002/2017JC012954

Shchepetkin, A. F., and McWilliams, J. C. J. O. M. (2005). The regional oceanic modeling system (ROMS): a split-explicit, free-surface, topography-following-coordinate oceanic model. *Ocean Modelling* 9, 347–404. doi: 10.1016/j.ocemod.2004.08.002

Sheu, D. D., Chou, W.-C., Wei, C.-L., Hou, W.-P., Wong, G. T. F., and Hsu, C.-W. (2010). Influence of El niño on the sea-to-air CO2 flux at the SEATS time-series site, northern south China Sea. *J. Geophys. Res.: Ocean.* 115, C10021. doi: 10.1029/2009JC006013

Sutton, A. J., Wanninkhof, R., Sabine, C. L., Feely, R. A., Cronin, M. F., and Weller, R. A. (2017). Variability and trends in surface seawater pCO_2 and CO_2 flux in the pacific ocean. *Geophys. Res. Lett.* 44, 5627–5636. doi: 10.1002/2017gl073814

Takahashi, T., Olafsson, J., Goddard, J., Chipman, D., and Sutherland, S. (1993). Seasonal variation of CO2 and nutrients in the high-latitude surface oceans: a comparative study. *Global Biogeochem. Cycles* 7, 843–878. doi: 10.1029/93GB02263

Takahashi, T., Sutherland, S. C., Sweeney, C., Poisson, A., Metzl, N., Tilbrook, B., et al. (2002). Global sea–air CO2 flux based on climatological surface ocean pCO2, and seasonal biological and temperature effects. *Deep Sea Res. Part II: Top. Stud. Oceanog.* 49, 1601–1622. doi: 10.1016/S0967-0645(02)00003-6

Takahashi, T., Sutherland, S. C., Wanninkhof, R., Sweeney, C., Feely, R. A., Chipman, D. W., et al. (2009). Climatological mean and decadal change in surface ocean pCO2, and net sea–air CO2 flux over the global oceans. *Deep Sea Res. Part II: Top. Stud. Oceanog.* 56, 554–577. doi: 10.1016/j.dsr2.2008.12.009

Tian, F., Zhang, R.-H., and Wang, X. (2019). Factors affecting interdecadal variability of air–sea CO2 fluxes in the tropical pacific, revealed by an ocean physical–biogeochemical model. *Climate Dynam.* 53, 3985–4004. doi: 10.1007/s00382-019-04766-5

Valsala, V., and Murtugudde, R. (2015). Mesoscale and intraseasonal air-sea CO2 exchanges in the western Arabian sea during boreal summer. *Deep Sea Res. Part I: OceanograpH. Res. Pap.* 103, 101–113. doi: 10.1016/j.dsr.2015.06.001

Wang, G., Shen, S. S. P., Chen, Y., Bai, Y., Qin, H., Chen, B., et al. (2020). Feasibility of reconstructing the basin-scale sea surface partial pressure of carbon dioxide from sparse *in situ* observations over the south china sea. *Earth Syst. Sci. Data* 13, 15. doi: 10.5194/essd-2020-167

Wong, G. T. F., Ku, T.-L., Mulholland, M., Tseng, C.-M., and Wang, D.-P. (2007). The SouthEast Asian time-series study (SEATS) and the biogeochemistry of the south China Sea–an overview. *Deep Sea Res. Part II: Top. Stud. Oceanog.* 54, 1434–1447. doi: 10.1016/j.dsr2.2007.05.012

Wong, C. S., Waser, N. A. D., Nojiri, Y., Johnson, W. K., Whitney, F. A., Page, J. S. C., et al. (2002). Seasonal and interannual variability in the distribution of surface nutrients and dissolved inorganic carbon in the northern north pacific: influence of El niño. *J. Oceanog.* 58, 227–243. doi: 10.1023/A:1015897323653

Xiao, F., Wang, D., and Leung, M. Y. T. (2020). Early and extreme warming in the south China Sea during 2015/2016: role of an unusual Indian ocean dipole event. *Geophys. Res. Lett.* 47, e2020GL089936. doi: 10.1029/2020gl089936

Xiao, F., Wang, D., Zeng, L., Liu, Q.-Y., and Zhou, W. (2019). Contrasting changes in the sea surface temperature and upper ocean heat content in the south China Sea during recent decades. *Climate Dynam.* 53, 1597–1612. doi: 10.1007/s00382-019-04697-1

Xiao, F., Zeng, L., Liu, Q.-Y., Zhou, W., and Wang, D. (2017). Extreme subsurface warm events in the south China Sea during 1998/99 and 2006/07: observations and mechanisms. *Climate Dynam.* 50, 115–128. doi: 10.1007/s00382-017-3588-y

Xie, S.-P., Xie, Q., Wang, D., and Liu, W. T. (2003). Summer upwelling in the south China Sea and its role in regional climate variations. *J. Geophys. Res.: Ocean.* 108, 3261. doi: 10.1029/2003JC001867

Xiu, P., and Chai, F. (2013). Connections between physical, optical and biogeochemical processes in the pacific ocean. *Prog. Oceanog.* 122, 30–53. doi: 10.1016/j.pocean.2013.11.008

Xiu, P., and Chai, F. (2014). Variability of oceanic carbon cycle in the north pacific from seasonal to decadal scales. *J. Geophys. Res.: Ocean.* 119, 5270–5288. doi: 10.1002/2013jc009505

Xu, F.-H., and Oey, L.-Y. (2015). Seasonal SSH variability of the northern south China Sea. *J. Phys. Oceanog.* 45, 1595–1609. doi: 10.1175/JPO-D-14-0193.1

Xue, H., Chai, F., Pettigrew, N., Xu, D., Shi, M., and Xu, J. (2004). Kuroshio intrusion and the circulation in the south China Sea. *J. Geophys. Res.: Ocean.* 109, C02017. doi: 10.1029/2002JC001724

Yang, B., and Byrne, R. (2022). Sub-Annual and inter-annual variations of total alkalinity in the northeastern gulf of Mexico. *Mar. Chem.* 104195. doi: 10.1016/j.marchem.2022.104195

Yu, Y., Zhang, H.-R., Jin, J., and Wang, Y. (2019). Trends of sea surface temperature and sea surface temperature fronts in the south China Sea during 2003–2017. *Acta Oceanol. Sin.* 38, 106–115. doi: 10.1007/s13131-019-1416-4

Yuan, Y. C., Liu, Y., Liao, G., Lou, R. Y., Su, J., and Wang, K. S. (2005). Calculation of circulation in the south China Sea during summer of 2000 by the modified inverse method. *Acta Oceanol. Sin.* 24, 14–30.

Zhu, X., Wang, H., Liu, G., Régnier, C., Kuang, X., Wang, D., et al. (2016). Comparison and validation of global and regional ocean forecasting systems for the south China Sea. *Natural Haz. Earth Syst. Sci.* 16, 1639–1655. doi: 10.5194/nhess-16-1639-2016

Zhu, X., Zu, Z., Ren, S., Zhang, M., Zhang, Y., Wang, H., et al. (2022). Improvements in the regional south China Sea operational oceanography forecasting system (SCSOFSv2). *Geoscientific Model. Dev.* 15, 995–1015. doi: 10.5194/gmd-15-995-2022